

A route to metalloligands consolidated silver nanoclusters by grafting thiocalix[4]arene onto polyoxovanadates

Received: 10 May 2023

Zhi Wang  ^{1,2}, Yan-Jie Zhu ^{1,2}, Bao-Liang Han ¹, Yi-Zhi Li ¹, Chen-Ho Tung ¹ & Di Sun  

Accepted: 22 August 2023

Published online: 31 August 2023

 Check for updates

Metalloligands provide a potent strategy for manipulating the surface metal arrangements of metal nanoclusters, but their synthesis and subsequent installation onto metal nanoclusters remains a significant challenge. Herein, two atomically precise silver nanoclusters $\{\text{Ag}_{14}[(\text{TC4A})_6(\text{V}_9\text{O}_{16})](\text{CyS})_3\}$ (Ag14) and $\{\text{Ag}_{43}\text{S}[(\text{TC4A})_2(\text{V}_4\text{O}_9)]_3(\text{CyS})_9(\text{PhCOO})_3\text{Cl}_3(\text{SO}_4)_4(\text{DMF})_3\cdot6\text{DMF}\}$ (Ag43) are synthesized by controlling reaction temperature ($\text{H}_4\text{TC4A} = p$ -tert-butyl-thiocalix[4]arene). Interestingly, the 3D scaffold-like $[(\text{TC4A})_6(\text{V}_9\text{O}_{16})]^{11-}$ metalloligand in Ag14 and 1D arcuate $[(\text{TC4A})_2(\text{V}_4\text{O}_9)]^{16-}$ metalloligand in Ag43 exhibit a dual role that is the internal polyoxovanadates as anion template and the surface TC4A^{4+} as the passivating agent. Furthermore, the thermal-induced structure transformation between Ag14 and Ag43 is achieved based on the temperature-dependent assembly process. Ag14 shows superior photothermal conversion performance than Ag43 in solid state indicating its potential for remote laser ignition. Here, we show the potential of two thiocalix[4]arene modified polyoxovanadates metalloligands in the assembly of metal nanoclusters and provide a cornerstone for the remote laser ignition applications of silver nanoclusters.

Silver nanoclusters (NCs) have been gaining attention due to their various applications in fields such as photoluminescence, catalysis, optical imaging, and biology^{1–4}. In recent years, the synthetic chemistry of silver NCs has advanced significantly through ligand engineering and template strategies, resulting in highly controllable and precise synthesis^{5,6}. The protective ligand is critical in determining the structure, stability, and properties of silver NCs. Organic ligands such as thiols, alkynes, and phosphines have been commonly used, and recent research has expanded to nitrogen-donor ligands, metalloligands, and macrocyclic hosts^{7–16}. Among these, metalloligands have brought opportunities for shaping ordered architectures and enhancing the stability of silver NCs. Zhang group reported a series of stable Ag–Ti NCs protected by a flexible trifurcate TiL_3 metalloligand, in which the TiL_3 moieties serve as the capping vertices of the silver NCs, thereby forming the tetrahedral geometry¹¹. Recently, our group successfully

achieved several Mo^{VI} -anchored thiocalix[4]arene metalloligands-protected silver NCs with different geometries through a stepwise assembly strategy, wherein it was demonstrated that the solvent controlled the cyclization of the metalloligand and then modulated the final silver NCs¹². It is apparent from the aforementioned results that the thiocalix[4]arene as a derivative of calixarene has phenolic hydroxyl groups and bridging sulfide groups, which again finds a niche for heterobimetallic cluster assembly^{17,18}.

Compared with transition metals (e.g., Cr, Mo, and W), vanadium is a multivalent redox-sensitive element that can exist in oxidation states ranging from -1 to $+5$, with the three highest oxidation states, $+3$, $+4$, and $+5$, being most common in the natural environment¹⁹. Polyoxovanadates (POVs) have unique characteristics that set them apart from polyoxometallates (POMs). They exhibit rich redox behavior, intriguing structural topologies, and flexible coordination patterns

¹School of Chemistry and Chemical Engineering, State Key Laboratory of Crystal Materials, Shandong University, Ji'nan 250100, People's Republic of China.

²These authors contributed equally: Zhi Wang, Yan-Jie Zhu.  e-mail: dsun@sdu.edu.cn

with secondary metal ions^{20,21}, making them excellent anion templates in the synthesis of silver NCs such as $[(V_{10}O_{28})@Ag_{50}]$, $[(V_{10}O_{28})@Ag_{44}]_n$ and $[(V_{10}O_{28})@Ag_{46}]_n$ ^{22,23}. In addition to being an anionic template, the inorganic POV_s can also be grafted by organic functional groups to form the hybrid POV_s that will further enrich the structural chemistry of silver NCs. Xie and coworkers synthesized a series of Ag–V hybrid NCs where phosphonate-modified oxovanadate building blocks or POV_s were revealed on the surface of the metal shell^{24–26}. Herein, we envisioned that integrating thiocalix[4]arenes and POV_s into an entity can provide the dual function of multi-dentate chelating of thiocalix[4]arenes and anionic templating of POV_s, leading to the emergence of richer coordination patterns and assembly phenomena than using organic ligands.

In this work, two silver NCs of $\{Ag_{14}[(TC4A)_6(V_9O_{16})](CyS)_3\}$ (**Ag14**) and $\{Ag_{43}S[(TC4A)_2(V_4O_9)]_3(CyS)_3(PhCOO)_3Cl_3(SO_4)_4(DMF)_3\cdot6DMF\}$ (**Ag43**) consolidated by 3D and 1D TC4A⁴⁺-POVs metalloligands are isolated by adjusting the solvothermal reaction temperature under otherwise identical conditions and characterized by single crystal X-ray diffraction (SCXRD) ($H_4TC4A = p$ -tert-butylthiocalix[4]arene). The two TC4A⁴⁺-POVs metalloligands successfully integrate the dual role of classical metalloligand and anion template, which were previously unobserved in the realm of both silver NCs and POMs chemistry. The structural conversion from **Ag43** to **Ag14** can be achieved by only adjusting temperature, whereas the reverse structural conversion needs stimuli from both temperature adjustment and reactant additives. Moreover, **Ag14** possesses superior photothermal conversion performance, which shows promising applications in laser ignition materials and photothermal therapy.

Results

Synthesis discussion

The mixture of H_4TC4A , $VOSO_4 \cdot xH_2O$, and $PhCOOAg$ was dispersed in DMF (*N*, *N*-dimethylformamide) and underwent solvothermal reaction to evaluate the feasibility of the TC4A⁴⁺-POVs metalloligands in the assembly of silver NCs. However, only a simple metal complex $\{Ag_2(TC4A\text{-VO})_2(DMF)_2\cdot6DMF\}$ (**Ag2**) was obtained under the above system, which indicates the possibility of the metalloligand as an ideal candidate for heterobimetallic assembly (Supplementary Fig. 1). Moreover, previously reported oxovanadium H_4TC4A complexes such as $PPh_4[(H_2TC4A)VOCl_2]$, $(PPh_4)_2\{[(H_2TC4A)V(O)(\mu\text{-}O)]_2\}$ and $PPh_4[(TC4A)V=O]$, etc. also suggested that the vanadium ion can ligate with H_4TC4A through phenolic hydroxyl oxygens and thioether groups (Supplementary Fig. 2)²⁷, which fully illustrated the diversity of the coordination modes of H_4TC4A with vanadium ions.

Motivated by the structure of **Ag2**, the auxiliary ligand of thiolate was introduced into the subsequent synthesis reactions. By varying the solvothermal reaction temperature, the pure phase of **Ag14** and a

mixed phase of **Ag14** and **Ag43** were obtained at 65 and 75 °C, respectively. Interestingly, we found 3D scaffold-like $[(TC4A)_6(V_9O_{16})]^{11-}$ metalloligand in **Ag14** and 1D arcuate $[(TC4A)_2(V_4O_9)]^{6-}$ metalloligand in **Ag43** (Fig. 1). To investigate the effect of temperature on the assembly, solvothermal reactions were performed in the range of 65–120 °C (Supplementary Fig. 3). Interestingly, **Ag14** can form in the wide temperature range of 65–120 °C whereas the mixture of **Ag14** and **Ag43** was found in the narrow temperature range of 75–80 °C. In spite of many attempts, the pure phase of **Ag43** cannot be obtained by simple temperature manipulation. Benefiting from the obviously different shapes, the clump-like **Ag14** and block-like **Ag43**, we can readily separate them manually under the microscope. Apparently, temperature has significant effects on the coordination-driven assembly process of two silver NCs, providing possibilities for thermal-induced structure transformation. Combining the reaction temperature as well as the compositions of the two silver NCs, the structure transformation of two silver NCs was successfully achieved by thermal stimulus. In addition, the vanadium source in the synthesis of **Ag14** is non-specific, as evidenced by the successful crystallization of **Ag14** after solvothermal reaction using other vanadium regents, such as $NaVO_3$ or Na_3VO_4 under otherwise identical conditions. The crystallography-related information and other characterizations, including infrared (IR) spectroscopy, ultraviolet-visible (UV-Vis) spectroscopy, and energy dispersive spectroscopy (EDS), are collected in Supplementary Figs. 4–32 and Supplementary Tables 1 and 2.

X-ray crystal structures

Ag14 and **Ag43** crystallized in the triclinic *P*–1 and trigonal *R*–3 space groups, and the asymmetric units of two NCs contain the complete cluster and 1/3 of the complete cluster, respectively. As shown in Fig. 2a, **Ag14** contains 14 silver ions, one 3D scaffold-like $[(TC4A)_6(V_9O_{16})]^{11-}$ metalloligand and three CyS^- . The configuration of the inner POV_s and the binding feature of the interfacial macrocyclic TC4A⁴⁺ are intriguing in 3D $[(TC4A)_6(V_9O_{16})]^{11-}$ metalloligand. In detail, six V atoms are attached to the lower rim of TC4A⁴⁺ via V–O_{phenol} bonds and adopt an octahedral coordination pattern with two other oxygen atoms, one stemmed from the $\{VO_4\}$ tetrahedron and the other from a terminal oxygen atom, to form six TC4A-VO₂ units. These TC4A-VO₂ units are connected to the six oxygen atoms via a vertex-sharing pattern on two poles of the rod-like $[V_3O_{10}]^{5-}$ anion that consists of three vertex-sharing $\{VO_4\}$ tetrahedra, resulting in the formation of $[(TC4A)_6(V_9O_{16})]^{11-}$ (Fig. 2b). Here, each of the upper and lower poles of $[V_3O_{10}]^{5-}$ has three triangularly distributed $\{VO_6\}$ connected by rod-like $[V_3O_{10}]^{5-}$ by sharing vertices (Supplementary Fig. 4a). The V–O bond lengths of $\{VO_4\}$ and $\{VO_6\}$ lie in the range of 1.583–1.870 Å and 1.579–2.108 Å, respectively. From the top view, the two groups of $\{VO_6\}$ in the triangular geometry are not face-to-face but rotated about 18.8°

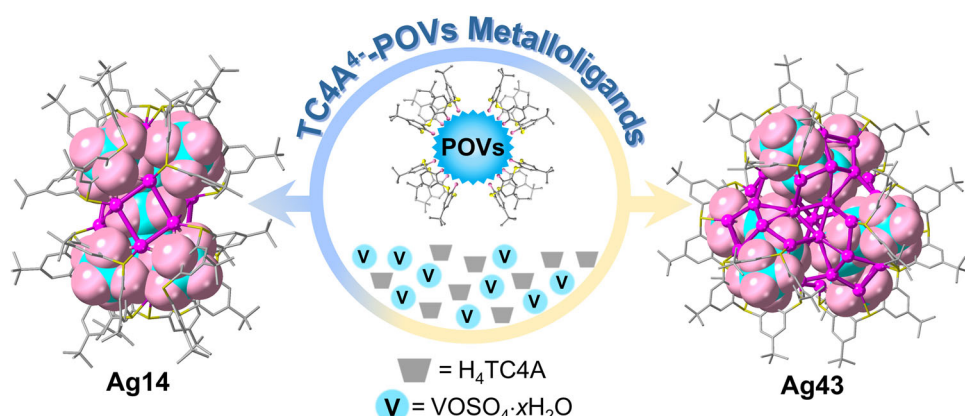


Fig. 1 | Description of TC4A⁴⁺-POVs metalloligands. Schematic diagram of the assembly of TC4A⁴⁺-POVs metalloligands, $H_4TC4A = p$ -tert-butylthiocalix[4]arene, POV_s = polyoxovanadates. Color labels: purple, Ag; yellow, S; gray, C; pink, O; cyan, V.

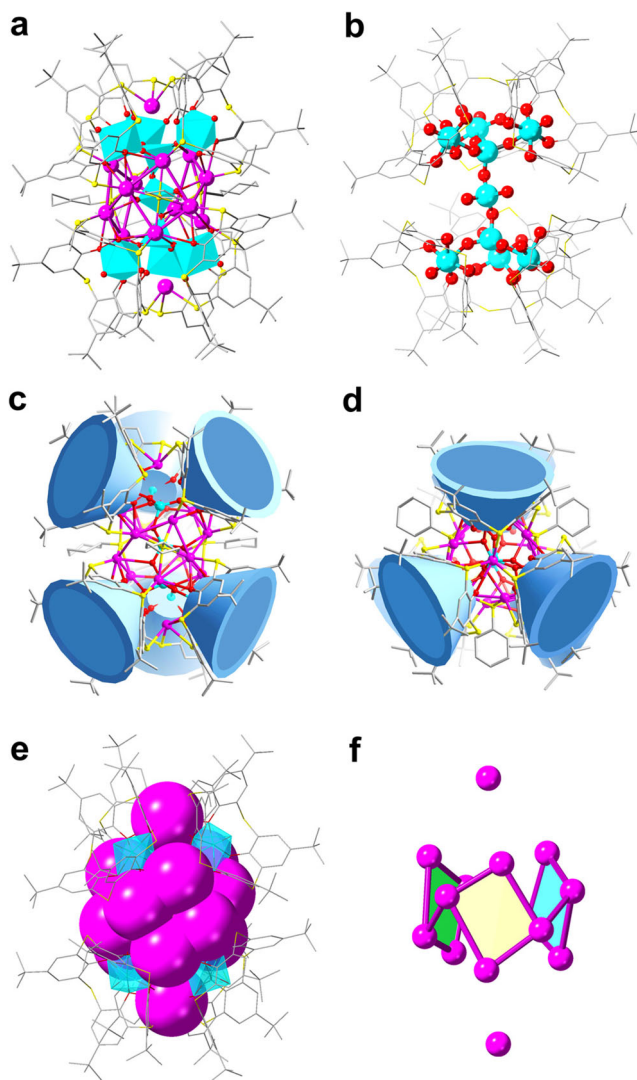


Fig. 2 | Molecular structure of the Ag14 resolved by SCXRD. **a** Total structure of the **Ag14**; **b** the structure of 3D scaffold-like $[(\text{TC4A})_6(\text{V}_9\text{O}_{16})]^{11-}$ metalloligand; **c** the side view (**d**) of the distribution of TC4A^{4+} in **Ag14**; **e** the Ag_{14} shell cemented by a 3D scaffold-like $[(\text{TC4A})_6(\text{V}_9\text{O}_{16})]^{11-}$ metalloligand; **f** the Ag_{14} silver shell. Color labels: purple, Ag; yellow, S; gray, C; red, O; cyan, V; cyan polyhedron, POVs; blue cup, TC4A^{4+} .

with respect to each other (Supplementary Fig. 4b), which causes the distortion of the outer silver shell and reduces the overall symmetry of the cluster. The coordination numbers of silver atoms in **Ag14** are three (1 Ag atom in AgS_2O , and 2 in AgS_3), four (4 in AgS_2O_2), and five (7 in AgS_2O_3).

Each group of three TC4A^{4+} is located at the upper and lower poles of **Ag14** (Fig. 2c, d). Notably, the 3D $[(\text{TC4A})_6(\text{V}_9\text{O}_{16})]^{11-}$ metalloligand runs through the silver shell and ligates all the silver atoms through Ag-S and Ag-O bonds (Supplementary Fig. 5). The waist of $[(\text{TC4A})_6(\text{V}_9\text{O}_{16})]^{11-}$ is surrounded by 12 silver atoms that resemble a silver crown consisting of three parallelograms connected through $\text{Ag}\cdots\text{Ag}$ interactions. The remaining two silver atoms suspended at the upper and lower parts of the silver crown are fixed in the center of the 3D scaffold by Ag-S bonds (Figs. 2e, f). Besides the 3D $[(\text{TC4A})_6(\text{V}_9\text{O}_{16})]^{11-}$ metalloligand, the 3 CyS^- exhibit μ_4 bonding mode capped on the Ag_{12} crown with the Ag-S bond lengths ranging from 2.440 to 2.718 Å (Supplementary Fig. 6).

As clarified in Fig. 3a, **Ag43** is composed of an Ag_{43} shell, an S^{2-} anion, three 1D arcuate $[(\text{TC4A})_2(\text{V}_4\text{O}_9)]^{6-}$ metalloligands, the organic

and inorganic mixed ligand shell of 9 CyS^- , 3 PhCOO^- , 4 SO_4^{2-} , 3 Cl^- , and three coordinated DMF molecules. The neutral **Ag43** has C_3 symmetry with the crystallographic C_3 axis passing through the Ag_{15} , S^{2-} and SO_4^{2-} (Supplementary Fig. 7). No sulfur-releasing reagent was added to the reaction, so the S^{2-} was probably derived from the $(\text{CySAg})_n$ precursor²⁸. **Ag43** has intriguing interfacial binding profiles resulting from the synergistic coordination of 1D arcuate metalloligands and other auxiliary ligands. The structure of the 1D arcuate metalloligand is disparate to that found in **Ag14**, where two TC4A-VO_2 units are connected by a $\{\text{V}_2\text{O}_7\}$ ($\text{V}-\text{O}$: 1.646–1.820 Å) by sharing vertices (Supplementary Fig. 8). Specifically, the structure of **Ag43** can be described as three 1D arcuate metalloligands ligating 15 silver atoms to form Ag_{15} caps, which are fused by sharing silver vertices (black atoms) to form an Ag_{42} metallic skeleton that further traps an Ag_{15} (purple atom) atom situated on the crystallographic C_3 axis to build the final **Ag43** shell ($\text{Ag}\cdots\text{Ag}$ distances: 2.910–3.242 Å) (Fig. 3b). The interior of the **Ag43** shell is further reinforced by an S^{2-} anion in a μ_7 coordination pattern and the surface coordination vacancies are filled with other auxiliary ligands. In detail, the silver shell of **Ag43** is shamrock-shaped, with the cavity large enough to accommodate three $\{\text{V}_4\text{O}_9\}$ acting as anion templates (Figs. 3c, d), and six TC4A^{4+} are combined in pairs by $\{\text{V}_4\text{O}_9\}$ and divided into three groups evenly arranged around **Ag43** shell (Figs. 3e, f). Three PhCOO^- adopt the unified $\mu_3\kappa^2\kappa^1$ coordination mode toward silver atoms to fill in the interstice between two TC4A^{4+} in the 1D arcuate metalloligand (Ag-O distances: 2.332–2.445 Å) (Supplementary Fig. 9), realizing the reinforcement of the periphery of the **Ag43** shell. Nine CyS^- ligands surround the periphery of the **Ag43** shell in μ_4 coordination mode, with six of them locating around the PhCOO^- ligands and the remaining three capping on the interspace between three 1D arcuate metalloligands (Supplementary Fig. 10). In addition, the region of the **Ag43** shell near to the C_3 axis is further cemented by inorganic anions of SO_4^{2-} and Cl^- . The SO_4^{2-} anion passing through the crystallographic C_3 axis adopts $\mu_6\kappa^3\kappa^1\kappa^1\kappa^1$ coordination mode toward Ag (Ag-O distances: 2.270–2.81 Å) and the other three SO_4^{2-} anions arranged in a triangular pattern adopt a unified $\mu_6\kappa^2\kappa^2\kappa^2$ mode (Ag-O distances: 2.264–2.684 Å) (Supplementary Fig. 11a). Each Cl^- anion on the surface of the silver shell is coordinate to five Ag atoms, acting as inorganic ligands and delivering complementary surface binding due to their small size (Supplementary Fig. 11b). Additionally, three DMF molecules are also involved in the stabilization of the silver shell. **Ag43** is protected by metalloligands, organic and inorganic mixed ligand shell, with the silver atoms forming the coordination numbers of three (three Ag atoms in AgS_2O , and three in AgSO_2), four (three in AgS_2O_2 , three in AgSO_2Cl , and three in AgS_2OCl), and five (nine in AgS_2O_3 , six in AgSO_3Cl , three in $\text{AgS}_2\text{O}_2\text{Cl}$, one in AgSO_3Cl , six in AgSO_4 , and three in AgS_2O_3).

Based on the above structural analysis, the reasons for **Ag14** can be obtained over a wide temperature range of 65–120 °C are summarized as follows: (i) The crystal structure of **Ag14** is simple, consisting of an Ag_{14} shell and binary ligand combination of $[(\text{TC4A})_6(\text{V}_9\text{O}_{16})]^{11-}$ metalloligand and CyS^- ; and (ii) The 3D scaffold-like $[(\text{TC4A})_6(\text{V}_9\text{O}_{16})]^{11-}$ metalloligand penetrating the cluster counteracts the local positive charge and increases the structural stability. Most silver NCs can only be isolated at a specific temperature or within a narrow temperature range, which requires high-precision temperature control equipment and synthesis conditions. On the other hand, silver NCs that can be obtained over a wide temperature range offer great advantages in their synthesis and applications. Furthermore, the most attractive aspects of **Ag14** and **Ag43** are the 3D scaffold-like $[(\text{TC4A})_6(\text{V}_9\text{O}_{16})]^{11-}$ metalloligand and 1D arcuate $[(\text{TC4A})_2(\text{V}_4\text{O}_9)]^{6-}$ metalloligand, respectively, which exhibit a dual role in the assembly process of two silver NCs: (i) inner POV part exerts the anion template effect; and (ii) the TC4A^{4+} on the surface as a passivator to stabilize the whole NC. In addition, all of the vanadium cations in both clusters are in their highest oxidation state of +5, which has a smaller ion radius as

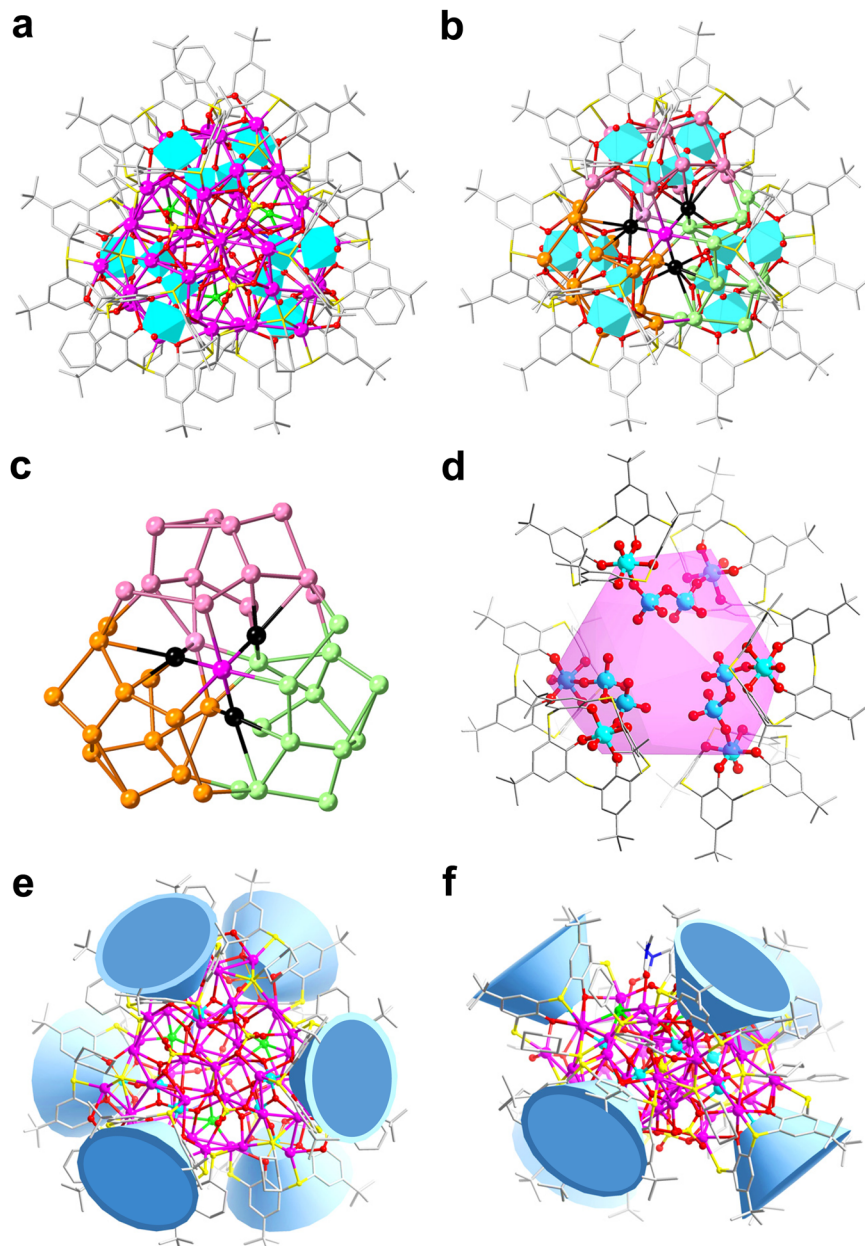


Fig. 3 | Molecular structure of the Ag43 resolved by SCXRD. **a** Total structure of the Ag43; **b** the Ag₄₃ shell cemented by three 1D arcuate metalloligands; **c** the Ag₄₃ shell in **(b)**, each Ag₁₅ caps highlighted individually by different colors (pink, orange and green), silver atoms shared between them highlighted by black atoms and Ag₁₅ atom passing through crystallographic C_3 axis highlighted by purple atom; **d** the

distribution of three 1D arcuate $[(\text{TC4A})_2(\text{V}_4\text{O}_9)]^{6-}$ metalloligands in Ag43, the purple shell represents silver shell; The top view **(e)** and the side view **(f)** of the distribution of TC4A⁴⁻ in Ag43. Color labels: purple, Ag; cyan, V; yellow, S; gray, C; red, O; green, Cl; blue, N; cyan polyhedron, POV; blue cup, TC4A⁴⁻.

well as higher charge density, as confirmed by the bond valence sum (BVS) calculation²⁹. The Ag...Ag interactions in Ag14 and Ag43 are both around 2.91–3.35 Å, which is larger than the sum of the Ag atom radii (2.89 Å) and shorter than the sum of the van der Waals radii (3.44 Å), indicating the oxidation state of silver is +1 rather than 0^{30,31}. Furthermore, we also demonstrated that all silver atoms in them are in +1 oxidation state by electrospray ionization mass spectrometry (ESI-MS; see below). The coordination process between V⁵⁺ cations and Ag⁺ cations with TC4A⁴⁻ is speculated to follow the hard-soft acid-base (HSAB) theory, where V⁵⁺ cations are oxygenophilic and readily coordinate to the deprotonated phenolic hydroxyl groups of TC4A⁴⁻, while Ag⁺ cations prefer to coordinate with thioether groups. The smaller radius of V⁵⁺ cations compared with, e.g., Nb, Ta, Mo, and W, allows them to adhere more easily to the bottom of the TC4A⁴⁻. To the best of

our knowledge, there are only sporadic reports of the high-nuclearity silver NCs protected by metalloligands (Supplementary Table 3). Upon comparison, we find that the mutable forms of POV in TC4A⁴⁻-POVs metalloligands provide more variability to their structure, which allowed two structurally different TC4A⁴⁻-POVs metalloligands to be obtained by adjusting the reaction temperature under otherwise identical conditions.

Structure transformation between Ag14 and Ag43

ESI-MS is a complementary characterization technique to X-ray crystallography for determining the chemical composition and charge state of metal NCs and is widely used to study their solution behavior^{32–37}. To investigate the assembly process of Ag14 and Ag43, we monitored the species in the reaction solution at 65–100 °C with

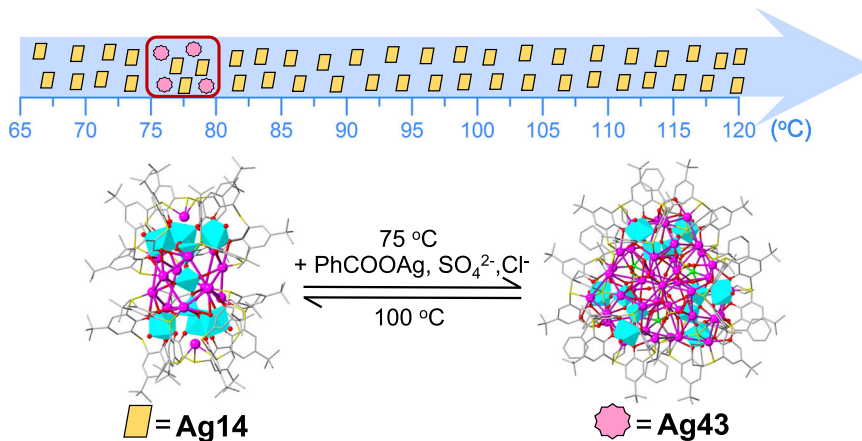


Fig. 4 | The structure transformation of Ag14 and Ag43. A schematic of the temperature-dependent assembly process and the structure transformation of **Ag14** and **Ag43**. Color labels: purple, Ag; yellow, S; gray, C; red, O; green, Cl; blue: N; cyan polyhedron, POVs.

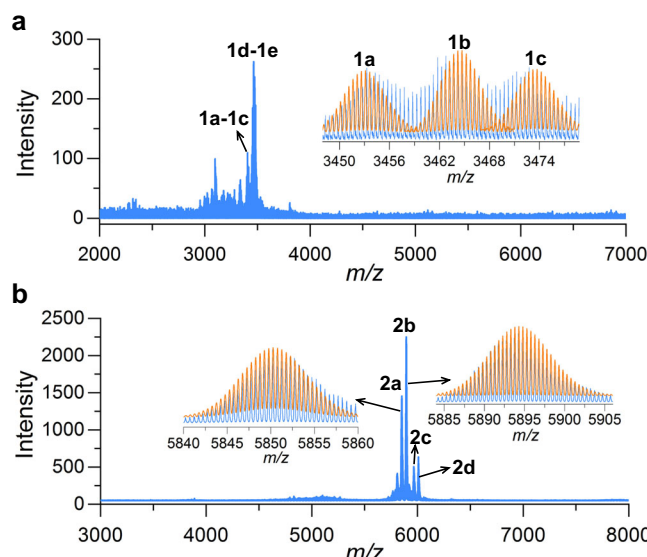


Fig. 5 | ESI-MS of Ag14 and Ag43. Positive ion mode ESI-MS of **Ag14** (a) and **Ag43** (b) dissolved in CH_2Cl_2 - CH_3OH mixed solvents. Insets: Zoom-in experimental (blue line) and simulated (orange line) isotope patterns of **1a-1c**, **2a**, and **2b** species.

5 °C intervals using ESI-MS while maintaining uniform instrumental test parameters for comparability of data (Supplementary Fig. 12). There were some species correlated to **Ag14** (Ag_{11} , Ag_{14} , Ag_{16}) at 65–100 °C and Ag_{47} species emerged only at 75–80 °C. The latter can be seen as a bigger congener of **Ag43** by appending a PhCOOAg , three Ag^+ , and solvent molecules. The simulated isotope distributions of **a-f** are shown in Supplementary Fig. 13. These ESI-MS data and synthesis experiments discussed above fully demonstrated that the assembly of **Ag14** and **Ag43** is sensitive to temperature, therefore, there is a promise for the structure transformation of **Ag14** and **Ag43** by thermal induction.

As expected, **Ag14** can be obtained by heating **Ag43** in DMF at 100 °C. However, the transformation from **Ag14** to **Ag43** cannot be achieved by simply changing temperature. By comparing the structures of two NCs, we found the composition of **Ag43** has additional PhCOO^- , SO_4^{2-} , and Cl^- , thus the transformation from **Ag14** to **Ag43** may require the addition of PhCOO^- , SO_4^{2-} , and Cl^- intentionally except for the change of temperature. We added crystals of **Ag14** to DMF and added an excess of PhCOO^- , SO_4^{2-} , and Cl^- to facilitate the transformation reaction, and finally obtained **Ag43** by solvothermal

reaction at 75 °C (Fig. 4)³⁸. Based on the above results, we believe that the structure transformation between two NCs should suffer from a structure breakage-reorganization route by thermal induction.

In addition to investigating the species in reaction solution at different temperatures by ESI-MS, the solution behavior of **Ag14** and **Ag43** dissolved in CH_2Cl_2 - CH_3OH mixed solvents was also studied by ESI-MS in positive ion mode. As shown in Fig. 5a, two sets of bivalent charged peaks, **1a-1c** and **1d-1e**, were observed in the m/z range of 2000–7000. **1a-1c** consist of five +2 species, which can be assigned to $[\text{Ag14}-2\text{CyS}^- + \text{DMF} + 2\text{CH}_3\text{OH}]^{2+}$ (**1a**), $[\text{Ag14}-2\text{CyS}^- + 2\text{CH}_2\text{Cl}_2]^{2+}$ (**1b**), $[\text{Ag14}-2\text{CyS}^- + 2\text{CH}_2\text{Cl}_2 + \text{H}_2\text{O}]^{2+}$ (**1c**), $[\text{Ag14} + \text{Ag}^+-\text{CyS}^- + 2\text{CH}_3\text{OH}]^{2+}$ (**1d**), and $[\text{Ag14} + \text{Ag}^+-\text{CyS}^- + 3\text{CH}_3\text{OH}]^{2+}$ (**1e**), respectively. It can be seen that **1a-1c** species are formed by stripping two CyS^- ligands from **Ag14**, but they still maintain the integrity of 14-nuclei silver framework and 3D $[(\text{V}_9\text{O}_{16})(\text{TC4A})_6]^{11-}$ metalloligand. All these assigned formulae are listed in Supplementary Table 4. The ESI-MS of **Ag43** has two primary peaks **2a** and **2b**, and both are +2 species (Fig. 5b). Peak **2a** centered at $m/z = 5850.1935$ can be identified to $[\text{Ag43}-2\text{PhCOO}^- + 2\text{H}_2\text{O}]^{2+}$ (calcd $m/z = 5850.3182$). Peak **2b** centered at $m/z = 5892.7112$ can be attributed to $[\text{Ag43}-2\text{PhCOO}^- + \text{CH}_2\text{Cl}_2 + 2\text{H}_2\text{O}]^{2+}$ (calcd $m/z = 5892.7942$) (Supplementary Table 5). Both **2a** and **2b** involve the dissociation of the two PhCOO^- ligands in solution but differ in the appended solvent molecules. By analyzing the species in ESI-MS of **Ag14** and **Ag43**, we found that both NCs are Ag(I) clusters and have high stability in CH_2Cl_2 - CH_3OH mixed solvents.

Of note, the intensity of **1d-1e** species is about 250 at a collision energy of 10 eV, while the intensity of **2b** species is about 2250 without collision energy at the same concentration (Supplementary Table 6). When **Ag14** was tested under the same operating parameters as **Ag43**, no peak emerged (Supplementary Fig. 14). These results indicated that **Ag43** is more easily ionized, which may be related to the labile PhCOO^- on the surface of **Ag43**.

Photoelectric response properties

The solid-state UV-Vis diffuse reflectance spectra of **Ag14** and **Ag43** were measured at room temperature in the wavelength range from 200 to 1100 nm (Supplementary Fig. 15). Both of them exhibit a broad absorption spanning ultraviolet and visible regions: one centered at 345 nm and the other at 338 nm. The low-energy broad absorption band is assigned to ligand-to-metal charge transfer, and the high-energy absorption peak is tentatively attributed to the ligand-based absorption. The band gaps of **Ag14** and **Ag43** are 1.78 and 1.70 V, respectively, as determined by the Kubelka-Munk function and Tauc plot³⁹. Considering the narrow band gap and wide absorption, the

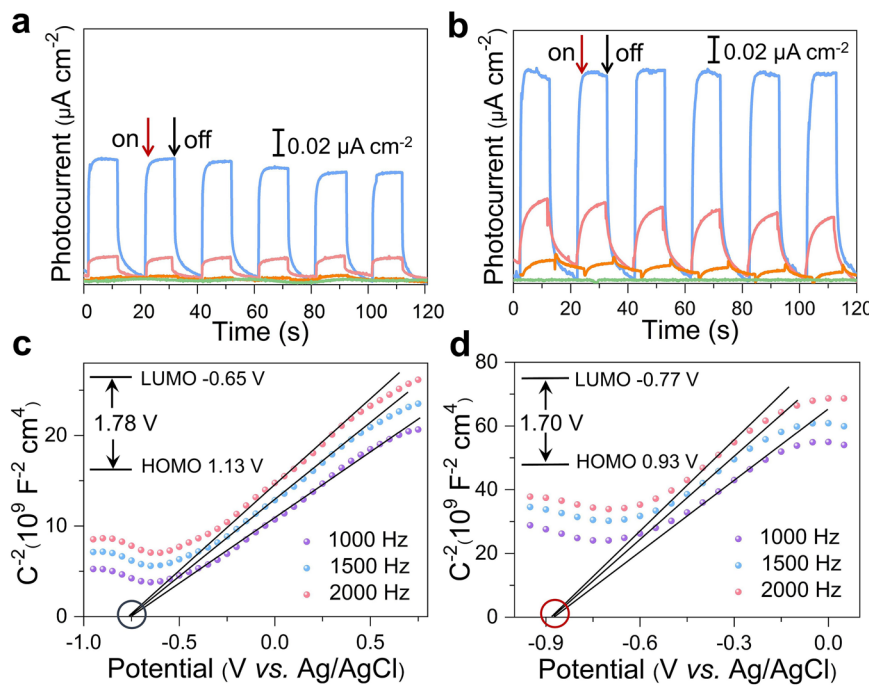


Fig. 6 | Photocurrent responses of **Ag14 and **Ag43**.** Photocurrent responses of **Ag14** (a) and **Ag43** (b) modified electrodes under repetitive light irradiation of different wavelengths (blue line, 365 nm; pink line, 420 nm; orange line, 495 nm;

green line, 570 nm). Mott–Schottky (M–S) plots of **Ag14** (c) and **Ag43** (d) modified electrodes at different frequencies.

photoelectrochemical properties of two silver NCs were further tested in a typical three-electrode system^{20,39}. With on-off cycling irradiation of different monochrome LED light ($\lambda = 365, 420, 495$, and 570 nm; 50 W; intervals of 10 s), both **Ag14** and **Ag43** exhibit the maximum photocurrent densities under 365 nm irradiation (Fig. 6a, b), and the photocurrent density decreased with increasing wavelength of the irradiation light, which is consistent with their strong absorption at 365 nm. The photocurrent density of **Ag43** ($0.1 \mu\text{A cm}^{-2}$) under 365 nm irradiation was twice that of **Ag14** ($0.05 \mu\text{A cm}^{-2}$), indicating that **Ag43** has better generation and separation efficiency of photoinduced electrons/holes pairs⁴⁰.

Mott–Schottky (M–S) measurements were performed using the impedance technique at the frequencies of 1000, 1500, and 2000 Hz to gain a better understanding of the semiconducting nature of **Ag14** and **Ag43** (Fig. 6c, d). The positive slope of the M–S plots proved the *n*-type semiconductor behavior of **Ag14** and **Ag43**⁴⁰. The flat band potential (E_{FB}) of *n*-type semiconductors is equal to the Fermi level estimated from the extrapolation of the M–S plots⁴¹. The conduction band potential (LUMO) of **Ag14** and **Ag43** is -0.65 and -0.77 V vs. normal hydrogen electrode (NHE), respectively. Moreover, the valence band potential (HOMO) of **Ag14** and **Ag43** is calculated to be 1.13 and 0.93 V vs. NHE, respectively, on the basis of the band gap energy obtained from UV–Vis diffuse reflectance spectra.

Photothermal conversion studies

The energy transition in the photophysical process is mainly illustrated by Jablonski diagram⁴², which contains the following several processes: excitation (or absorption), vibrational relaxation (heat), radiative emission (fluorescence), and non-radiative transition (heat) (Supplementary Fig. 16)^{43,44}. For **Ag14** and **Ag43**, no fluorescence was observed under 660 nm laser irradiation, indicating that the radiative migration was very weak and photothermal conversion became the main energy release route^{45,46}. Therefore, their photothermal conversion performance was investigated both in the crystalline and solution states. As shown in Fig. 7a, the temperature of **Ag14** crystals reached 194°C in 1.5 s under 660 nm laser irradiation (0.9 W cm^{-2}) at a distance of 20 cm.

Surprisingly, the heating rate (115°C s^{-1}) of **Ag14** is much higher than that of other reported silver NC **SD/Ag18a** (8.2°C s^{-1} , 660 nm, 0.9 W cm^{-2}) (Supplementary Fig. 17) and most of the reported silver nanomaterials (Supplementary Table 7)^{12,47–49}. Compared with **Ag14**, the heating rate of **Ag43** is slower, with the temperature reaching 105°C in 1.5 s ($55.3^\circ\text{C s}^{-1}$), and the maximum temperature is only 141°C under the same condition (Fig. 7a). As we have mentioned above, the channels of radiative decay of two NCs are almost suppressed. It is speculated that absorption may be the main factor influencing the photothermal conversion performance, and **Ag14** has stronger absorption at 660 nm than **Ag43** (Supplementary Fig. 15a), therefore, **Ag14** can harvest more energy and produce higher temperature under 660 nm laser irradiation.

The aforementioned results indicate that **Ag14** has the potential to be a remote laser ignition material. The flammable material match was chosen as the research model. The measurement range of the thermal imaging camera is $0–650^\circ\text{C}$; when the temperature is higher than 650°C , it can only display 650°C . As shown in Fig. 7b, the match coated with 2 mg **Ag14** (hereafter abbreviated as **Ag14/match**) was ignited within 1 s under 660 nm laser irradiation (0.9 W cm^{-2}) at a distance of 50 cm, while the match could not be ignited within 3 min under the same condition. Next, the ignition time was investigated by changing the laser power and the irradiation distance, respectively. The **Ag14/match** can be successfully ignited at the laser power range of 0.2 to 0.6 W cm^{-2} at a distance of 20 cm (Fig. 7c). However, the time to ignite the match is much longer than that of **Ag14/match** under the same conditions, and the match cannot be ignited when the laser power is below 0.4 W cm^{-2} (Fig. 7d, e). The time to ignite the **Ag14/match** became longer as the distance changing from 10 cm to 40 cm at laser power of 0.4 W cm^{-2} , while match cannot be ignited when the distance exceeds 20 cm (Supplementary Fig. 18, Fig. 7f). On the basis of the above experiments, it can be concluded that the ignition time and the threshold laser power can be significantly reduced by coating the match with **Ag14**, suggesting that **Ag14** has the potential to be used as laser igniter for realizing remote laser ignition and controlled explosion^{50–52}.

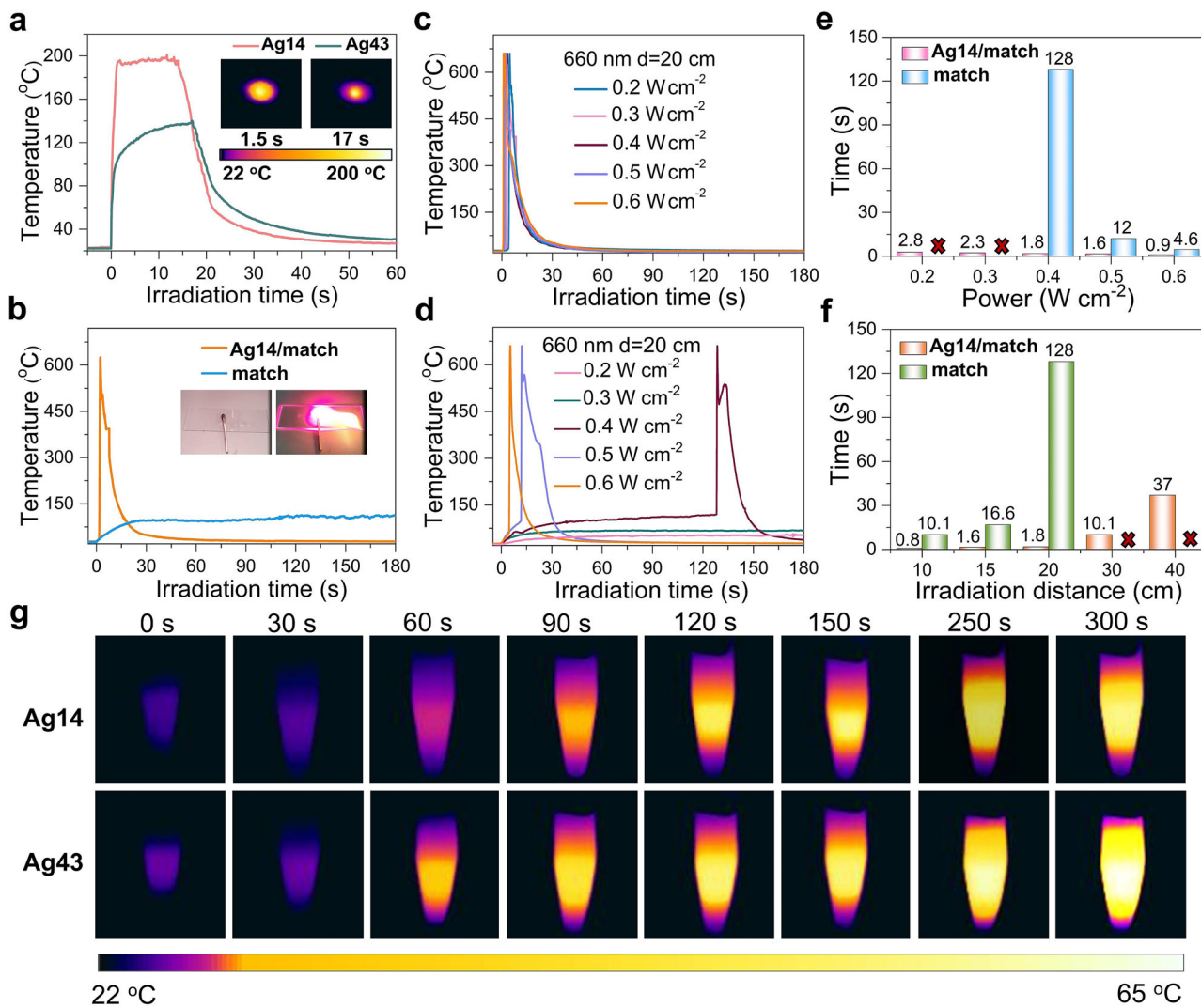


Fig. 7 | Photothermal conversion performance of Ag14 and Ag43.

a Photothermal conversion of **Ag14** and **Ag43** crystals under 660 nm laser irradiation (0.9 W cm^{-2}). Insets: thermal images of **Ag14** and **Ag43** crystals at the highest temperature. **b** The plots of temperature evolution vs. irradiation time for **Ag14/match** and **match** under 660 nm laser irradiation (0.9 W cm^{-2}) at a distance of 50 cm. Insets: photos of **Ag14/match** and ignition. The plots of temperature

evolution vs. irradiation time for **Ag14/match** (**c**) and **match** (**d**) with different laser powers at a distance of 20 cm. The comparison of the ignition time of **Ag14/match** and **match** at different laser power (**e**) and distance (**f**), the numbers in the figure represent the ignition time, and the red cross mean it cannot be ignited. **g** Thermal images of the CHCl_3 solutions of **Ag14** and **Ag43** at the concentration of $200 \mu\text{M}$ under 660 nm laser irradiation (0.9 W cm^{-2}).

Furthermore, their photothermal conversion performance in solution was investigated. The temperature evolutions of the CHCl_3 solutions of **Ag14** and **Ag43** were recorded by the thermal imaging camera under 660 nm laser irradiation (0.9 W cm^{-2}) at concentrations of 50, 100, and $200 \mu\text{M}$. The thermal imaging photographs show the photothermal effect of the CHCl_3 solutions of **Ag14** and **Ag43** at the concentration of $200 \mu\text{M}$ in a centrifuge tube (Fig. 7g). The maximum photothermal temperature of **Ag43** could reach 60.0°C , which was 3.8°C higher than that of **Ag14** (56.2°C) (Supplementary Fig. 19). This may be due to that the UV-Vis absorption intensity of **Ag43** at 660 nm is higher than that of **Ag14** at the same concentration (Supplementary Fig. 20)^{53,54}. The photothermal conversion efficiency (η) values of the CHCl_3 solutions of **Ag14** and **Ag43** were 45.69% and 33.87%, respectively, at a concentration of $200 \mu\text{M}$ under 660 nm laser irradiation (Supplementary Figs. 21 and 22)⁵⁵. The CHCl_3 solution of **Ag14** has a high η compared to the reported four Ag_{16} NCs (41.1%, 35.8%, 40.7%, and 33.6%) as well as dopamine-melanin colloidal nanospheres (40%)^{47,56}. Moreover, the maximum temperatures increased with increasing concentrations of **Ag14** and **Ag43** and remained almost constant in five cycles of the heating and

cooling process (Supplementary Fig. 23). These results indicated that the solutions of the two silver NCs have good photothermal conversion performance, making them potentially applicable in bio-imaging and photothermal therapy. The compared UV-Vis spectra of fresh samples and samples stored in ambient conditions for 6 months and the photothermal heating and cooling process confirmed that **Ag14** and **Ag43** exhibit high stability to light and air both in the solid and solution states (Supplementary Figs. 15a and 24).

Discussion

In summary, we showcase an efficient strategy to synthesize two silver NCs consolidated by 3D scaffold-like $[(\text{TC4A})_6(\text{V}_9\text{O}_{16})]^{11-}$ and 1D arcuate $[(\text{TC4A})_2(\text{V}_4\text{O}_9)]^{10-}$ metalligands. Although there has been extensive research on organic-inorganic hybrid POV, this work represents the study targeting two organic ligand-modified POV as metalligands for the stabilization of silver NCs utilizing multiple-site and multiple-dentate (MSMD) coordination patterns. On the other hand, TC4A^{4-} -POVs hybrids with dual functionalities as internal anion template and external ligand have been proven to be reliable ligands for constructing multinuclear silver NCs. Noteworthy, the exceptional

photothermal conversion performance of **Ag14** makes it a promising material for remote laser ignition. The design and synthesis of metal-ligands present exciting challenges and offer a fertile platform for exploration, opening up opportunities for creativity in combining the esthetics of synthetic chemistry with self-assembly, which has the potential to drive further developments in the synthesis of silver NCs. Our research expands the scope of assembling macrocyclic thiocalix[4]arene ligands with POVs in a sensible manner and provides an avenue for further design and understanding metalloligands.

Methods

Synthesis of (CySag)_n

(CySag)_n was synthesized by the following reported procedure⁵⁷. Firstly, AgNO₃ (30 mmol, 5 g) was dissolved in 75 mL MeCN, and CySH (30 mmol, 3.66 mL) and Et₃N (36 mmol, 5 mL) were added into 100 mL EtOH. Then, the above two solutions were mixed and stirred for 5 h in the dark, and the light yellow powdery (CySag)_n was obtained with a yield of 90% (based on AgNO₃) by filtration of the above light yellow suspension. Selected IR peaks (cm⁻¹): 2920 (s), 1435 (m), 1269 (m), 998 (m), 719 (m) (Supplementary Fig. 25).

Synthesis of H₄TC4A

H₄TC4A was synthesized by the following reported procedure⁵⁸. Firstly, the mixture of *p*-tert-butylphenol (0.43 mol, 64.5 g), S₈ (0.86 mol, 27.5 g), and NaOH (0.215 mol, 8.86 g) was added to a 500 mL flask containing tetraethylene glycol dimethyl ether (19 mL) under nitrogen atmosphere. Then, the temperature was raised to 230 °C within 240 min and held for 180 min. The resulting hydrogen sulfide is removed by a slow flow of nitrogen during the reaction. After cooling to room temperature, ether (140 mL) and toluene (35 mL) were added to the flask to dilute the dark red product, and then the above solution was acidified with 4 M H₂SO₄ (140 mL) for 1 h. The precipitate was collected by filtration and recrystallized from CHCl₃ with a yield of 20% (based on *p*-tert-butylphenol). ¹H NMR (400 MHz, CDCl₃): δ = 9.60 (s, 4H, OH), 7.63 (s, 8H, Ar-H), 1.22 (s, 36H, C(CH₃)₃). Selected IR peaks (cm⁻¹): 3334 (m), 2962 (m), 1450 (s), 1397 (m), 1241 (s), 880 (m), 740 (s) (Supplementary Fig. 26).

Synthesis of Ag2

The synthesis of needle-black crystals of **Ag2** involves the following steps. Firstly, H₄TC4A (0.015 mmol, 10.8 mg), VOSO₄·xH₂O (0.05 mmol, 8 mg), and PhCOOAg (0.02 mmol, 4.6 mg) were dispersed in 1.5 mL DMF and the suspension was stirring (800 rpm) for 6 h at room temperature (20 °C). Then the mixture was sealed in a 25 mL Teflon-lined stainless autoclave and heated at 65 °C for 33 h. Black needle-like crystals of **Ag2** were collected with a yield of 15% after the solvothermal reaction (based on PhCOOAg). Elemental analyses calc. (found) for **Ag2** (C₈₉H₁₄₅Ag₂N₃O₃₁S₈V₂): C, 45.89 (47.68); H, 6.23 (5.586); N, 1.80 (1.66%). Selected IR peaks (cm⁻¹): 2951 (m), 2348 (m), 1647 (s), 1424 (s), 1251 (m), 1075 (m), 983 (m), 833 (m), 757 (m), 538 (m).

Synthesis of Ag14

Typically, H₄TC4A (0.015 mmol, 10.8 mg), VOSO₄·xH₂O (0.05 mmol, 8 mg), and PhCOOAg (0.1 mmol, 22.9 mg) were dissolved in 1.5 mL DMF. After stirring (800 rpm) at room temperature (20 °C) for 3 h, (CySag)_n (0.05 mmol, 11.4 mg) and NaCl (0.017 mmol, 1 mg) were added into above solution which is further treated for 3 h under the same stirring (800 rpm) condition. Then the mixture was sealed in a 25 mL Teflon-lined stainless autoclave and heated at 65 °C for 33 h. After cooling to room temperature, black clump-like crystals of **Ag14** were formed with a yield of 15% (based on H₄TC4A). The above synthetic reaction can readily achieve a tenfold scale-up and produce 20.6 mg **Ag14** in one batch. Elemental analyses calc. (found) for **Ag14** (C₂₇₃H₃₇₂Ag₁₄N₅O₆₅S₂₇V₉): C, 43.11 (40.72); H, 4.89 (4.311); N, 0.92

(0.94%). Selected IR peaks (cm⁻¹): 2953 (m), 2366 (m), 1678 (m), 1419 (s), 1260 (s), 1075 (m), 886(m), 821 (s), 758 (s), 686(s), 531(s).

Synthesis of Ag43

The synthesis of **Ag43** was similar to those described for **Ag14**. The only difference is the solvothermal reaction temperature, with the mixture of **Ag14** and **Ag43** being obtained between 75 and 80 °C at the solvothermal reaction. **Ag43** is a black block-like crystal with a yield of 7%, and **Ag14** with a yield of 10% (based on H₄TC4A). Elemental analyses calc. (found) for **Ag43** (C₃₄₂H₄₈₅Ag₄₃Cl₃N₉O₁₀₄S₃₈V₁₂): C, 31.66 (30.44); H, 3.70 (3.758); N, 0.97 (0.84%). Selected IR peaks (cm⁻¹): 2950 (m), 2362 (m), 1680 (s), 1416 (s), 1262 (m), 1076(m), 803(s), 708(s), 537 (m).

Data availability

The data that support the findings of this study are available within the article and its Supplementary Information files. Other relevant data are available from the corresponding author upon request. The X-ray crystallographic coordinates for structures reported in this article have been deposited at the Cambridge Crystallographic Data Center under deposition numbers CCDC: 2251154, 2251155, and 2251156 for **Ag2**, **Ag14**, and **Ag43**. These data can be obtained free of charge from the Cambridge Crystallographic Data Center via www.ccdc.cam.ac.uk/data_request/cif.

References

- Alhilaly, M. J. et al. [Ag₆₇(SPhMe₂)₃₂(PPh₃)₈]³⁺: synthesis, total structure, and optical properties of a large box-shaped silver nanocluster. *J. Am. Chem. Soc.* **138**, 14727–14732 (2016).
- Joshi, C. P., Bootharaju, M. S., Alhilaly, M. J. & Bakr, O. M. [Ag₂₅(SR)₁₈]: the “golden” silver nanoparticle. *J. Am. Chem. Soc.* **137**, 11578–11581 (2015).
- Narouz, M. R. et al. N-heterocyclic carbene-functionalized magic-number gold nanoclusters. *Nat. Chem.* **11**, 419–425 (2019).
- Zhao, Y. et al. A dual purpose strategy to endow gold nanoclusters with both catalysis activity and water solubility. *J. Am. Chem. Soc.* **142**, 973–977 (2020).
- Qu, M. et al. Bidentate phosphine-assisted synthesis of an all-alkynyl-protected Ag₇₄ nanocluster. *J. Am. Chem. Soc.* **139**, 12346–12349 (2017).
- Wang, Q. M., Lin, Y. M. & Liu, K. G. Role of anions associated with the formation and properties of silver clusters. *Acc. Chem. Res.* **48**, 1570–1579 (2015).
- Anson, C. E. et al. Synthesis and crystal structures of the ligand-stabilized silver chalcogenide clusters [Ag₁₅₄Se₇₇(dpppx)₁₈], [Ag₃₂₀(StBu)₆₀S₁₃₀(dppp)₁₂], [Ag₃₅₂S₁₂₈(StC₅H₁₁)₉₆], and [Ag₄₉₀S₁₈₈(StC₅H₁₁)₁₁₄]. *Angew. Chem. Int. Ed.* **47**, 1326–1331 (2008).
- Bootharaju, M. S. et al. Ag₄₄(EBT)₂₆(TPP)₄ nanoclusters with tailored molecular and electronic structure. *Angew. Chem. Int. Ed.* **60**, 9038–9044 (2021).
- Duan, G. X. et al. An atomically precise all-tert-butylethyne-protected Ag₅₁ superatom nanocluster with color tunability. *Nanoscale* **10**, 18915–18919 (2018).
- Yuan, S. F., Liu, W. D., Liu, C. Y., Guan, Z. J. & Wang, Q. M. Nitrogen donor protection for atomically precise metal nanoclusters. *Chem. Eur. J.* **28**, e202104445 (2022).
- Gao, M.-Y. et al. Tetrahedral geometry induction of stable Ag-Ti nanoclusters by flexible trifurcate TiL₃ metalloligand. *J. Am. Chem. Soc.* **142**, 12784–12790 (2020).
- Wang, Z. et al. Solvent-controlled condensation of [Mo₂O₅(PTC4A)₂]⁶⁻ metalloligand in stepwise assembly of hexagonal and rectangular Ag₁₈ nanoclusters. *Angew. Chem. Int. Ed.* **61**, e202200823 (2022).

13. Wang, Z. et al. Stepwise assembly of Ag_{42} nanocalices based on a Mo^{VI} -anchored thiocalix[4]arene metalloligand. *ACS Nano* **16**, 4500–4507 (2022).
14. Guan, Z.-J. et al. Thiocalix[4]arene: new protection for metal nanoclusters. *Sci. Adv.* **2**, e1600323 (2016).
15. Guan, Z.-J. et al. Ligand engineering toward the trade-off between stability and activity in cluster catalysis. *Angew. Chem. Int. Ed.* **61**, e202116965 (2022).
16. Guan, Z.-J. et al. The stability enhancement factor beyond eight-electron shell closure in thiocalix[4]arene-protected silver clusters. *Chem. Sci.* **10**, 3360–3365 (2019).
17. Hang, X., Yu, Y., Wang, Z. & Bi, Y. Thiocalixarene-supported MoNa clusters: crystal transition and Mo-S coordination on visible-light absorption. *Cryst. Growth Des.* **20**, 7934–7940 (2020).
18. Kumar, R., Lee, Y. O., Bhalla, V., Kumar, M. & Kim, J. S. Recent developments of thiocalixarene based molecular motifs. *Chem. Soc. Rev.* **43**, 4824–4870 (2014).
19. Shaheen, S. M. et al. Redox chemistry of vanadium in soils and sediments: interactions with colloidal materials, mobilization, speciation, and relevant environmental implications—a review. *Adv. Colloid Interface Sci.* **265**, 1–13 (2019).
20. Monakhov, K. Y., Bensch, W. & Kögerler, P. Semimetal-functionalised polyoxovanadates. *Chem. Soc. Rev.* **44**, 8443–8483 (2015).
21. Martin-Caballero, J. et al. A robust open framework formed by decavanadate clusters and copper(II) complexes of macrocyclic polyamines: permanent microporosity and catalytic oxidation of cycloalkanes. *Inorg. Chem.* **55**, 4970–4979 (2016).
22. Li, L. et al. A classical $[\text{V}_{10}\text{O}_{28}]^{6-}$ anion templated high-nucularity silver thiolate cluster. *Chem. Commun.* **58**, 9234–9237 (2022).
23. Wang, Z. et al. Enclosing classical polyoxometallates in silver nanoclusters. *Nanoscale* **11**, 10927–10931 (2019).
24. Xie, Y. P. & Mak, T. C. High-nucularity silver ethynide clusters assembled with phosphonate and metavanadate precursors. *Angew. Chem. Int. Ed.* **51**, 8783–8786 (2012).
25. Xie, Y. P. & Mak, T. C. Silver(I)-ethynide clusters constructed with phosphonate-functionized polyoxovanadates. *J. Am. Chem. Soc.* **133**, 3760–3763 (2011).
26. Xie, Y. P. & Mak, T. C. A Pyrovanadate-templated silver(I)-ethynide cluster circumscribed by macrocyclic polyoxovanadate(V). *Chem. Commun.* **48**, 1123–1125 (2012).
27. Hoppe, E. & Limberg, C. Oxovanadium(V) tetrathiacalix[4]arene complexes and their activity as oxidation catalysts. *Chem. Eur. J.* **13**, 7006–7016 (2007).
28. Li, G., Lei, Z. & Wang, Q. M. Luminescent molecular Ag-S nanocluster $[\text{Ag}_{62}\text{S}_{13}(\text{SBu}')_{32}](\text{BF}_4)_4$. *J. Am. Chem. Soc.* **139**, 12346–12349 (2017).
29. Liu, W. T. & Thorp, H. H. Bond valence sum analysis of metal-ligand bond lengths in metalloenzymes and model complexes. 2. refined distances and other enzymes. *Inorg. Chem.* **32**, 4102–4105 (1993).
30. Schmidbaur, H. & Schier, A. Argentophilic interactions. *Angew. Chem. Int. Ed.* **54**, 746–784 (2015).
31. Pykkö, P. Strong closed-shell interactions in inorganic chemistry. *Chem. Rev.* **97**, 597–636 (1997).
32. Dong, J. et al. Synthesizing photoluminescent $\text{Au}_{28}(\text{SC}_2\text{H}_5\text{Ph}-\text{t-Bu})_{22}$ nanoclusters with structural features by using a combined method. *Angew. Chem. Int. Ed.* **60**, 17932–17936 (2021).
33. Cao, Y. et al. Revealing the etching process of water-soluble Au_{25} nanoclusters at the molecular level. *Nat. Chem.* **12**, 3212 (2021).
34. Maman, M. P., Nair, A. S., Abdul Hakkim Nazeeja, A. M., Pathak, B. & Mandal, S. Synergistic effect of bridging thiolate and hub atoms for the aromaticity driven symmetry breaking in atomically precise gold nanocluster. *J. Phys. Chem. Lett.* **11**, 10052–10059 (2020).
35. Liu, Y., Najafabadi, B. K., Fard, M. A. & Corrigan, J. F. A functionalized Ag_2S molecular architecture: facile assembly of the atomically precise ferrocene-decorated nanocluster $[\text{Ag}_{74}\text{S}_{19}(\text{dppp})_6(\text{fcC}[O]\text{OCH}_2\text{CH}_2\text{S}_2)]_{18}$. *Angew. Chem. Int. Ed.* **127**, 4914–4917 (2015).
36. Shichibu, Y., Zhang, M., Kamei, Y. & Konishi, K. $[\text{Au}_7]^{3+}$: a missing link in the four-electron gold cluster family. *J. Am. Chem. Soc.* **136**, 12892–12895 (2014).
37. Chakraborty, I. & Pradeep, T. Atomically precise clusters of noble metals: emerging link between atoms and nanoparticles. *Chem. Rev.* **117**, 8208–8271 (2017).
38. Zeng, C., Liu, C., Pei, Y. & Jin, R. Thiol ligand-induced transformation of $\text{Au}_{38}(\text{SC}_2\text{H}_5\text{Ph})_{24}$ to $\text{Au}_{36}(\text{SPh-t-Bu})_{24}$. *ACS Nano* **7**, 6138–6145 (2013).
39. Tang, S.-Y. et al. Design of core-shell quantum dots-3D WS_2 nano-wall hybrid nanostructures with high-performance bifunctional sensing applications. *ACS Nano* **14**, 12668–12678 (2020).
40. Saha, S., Das, G., Thote, J. & Banerjee, R. Photocatalytic metal-organic framework from CdS quantum dot incubated luminescent metallohydrogel. *J. Am. Chem. Soc.* **136**, 14845–14851 (2014).
41. Hu, X. et al. Self-assembly of a semiconductive and photoactive heterobimetallic metal-organic capsule. *Angew. Chem. Int. Ed.* **60**, 10516–10520 (2021).
42. Qi, J. et al. Light-driven transformable optical agent with adaptive functions for boosting cancer surgery outcomes. *Nat. Commun.* **9**, 1848 (2018).
43. Pham, T.-T. D., Phan, L. M. T., Cho, S. & Park, J. Enhancement approaches for photothermal conversion of donor-acceptor conjugated polymer for photothermal therapy: a review. *Sci. Technol. Adv. Mater.* **23**, 707–734 (2022).
44. Feng, G., Zhang, G. Q. & Ding, D. Design of superior phototheranostic agents guided by Jablonski diagrams. *Chem. Soc. Rev.* **49**, 8179–8234 (2020).
45. Roper, D. K., Ahn, W. & Hoepfner, M. Microscale heat transfer transduced by surface plasmon resonant gold nanoparticles. *J. Phys. Chem. C* **111**, 3636–3641 (2007).
46. Link, S. & El-Sayed, M. A. Shape and size dependence of radiative, non-radiative and photothermal properties of gold nanocrystals. *Int. Rev. Phys. Chem.* **19**, 409–453 (2000).
47. Wang, H. H. et al. Monocarboxylate-protected two-electron superatomic silver nanoclusters with high photothermal conversion performance. *Nanoscale* **15**, 8245–8254 (2023).
48. Borah, R. & Verbruggen, S. W. Silver-gold bimetallic alloy versus core-shell nanoparticles: implications for plasmonic enhancement and photothermal applications. *J. Phys. Chem. C* **124**, 12081–12094 (2020).
49. Su, J. et al. Enhancing the photothermal conversion of tetrathiafulvalene-based MOFs by redox doping and plasmon resonance. *Chem. Sci.* **13**, 1657–1664 (2022).
50. Han, X. et al. Intensifying heat using MOF-isolated graphene for solar-driven seawater desalination at 98% solar-to-thermal efficiency. *Adv. Funct. Mater.* **31**, 2008904 (2021).
51. Wang, Q.-Y. et al. o-Carborane-based and atomically precise metal clusters as hypergolic materials. *J. Am. Chem. Soc.* **142**, 12010–12014 (2020).
52. De, N. N., Cummock, N. R., Gunduz, I. E., Tappan, B. C. & Son, S. F. Photoflash and laser ignition of select high-nitrogen materials. *Combust. Flame* **167**, 207–217 (2016).
53. Zada, S. et al. Algae extraction controllable delamination of vanadium carbide nanosheets with enhanced near-infrared photothermal performance. *Angew. Chem. Int. Ed.* **59**, 6601–6606 (2020).
54. Lyu, Y. et al. Enhancing both biodegradability and efficacy of semiconducting polymer nanoparticles for photoacoustic imaging and photothermal therapy. *ACS Nano* **12**, 1801–1810 (2018).
55. Gao, X. et al. Synthesis and near-infrared photothermal conversion of discrete supramolecular topologies featuring half-sandwich $[\text{Cp}^*\text{Rh}]$ units. *J. Am. Chem. Soc.* **143**, 17833–17842 (2021).

56. Liu, Y. et al. Dopamine-melanin colloidal nanospheres: an efficient near-infrared photothermal therapeutic agent for in vivo cancer therapy. *Adv. Mater.* **25**, 1353–1359 (2013).
57. Hong, S. H., Olin, Å. & Hesse, R. The crystal structure of silver(I) cyclohexanethiolate. *Acta Chem. Scand. A* **29**, 583–589 (1975).
58. Iki, N. et al. Synthesis of *p*-tert-butylthiacalix[4]arene and its inclusion property. *Tetrahedron* **56**, 1437–1443 (2000).

Acknowledgements

This work was financially supported by the National Natural Science Foundation of China (Grant Nos. 22201159 to Z.W., 22171164, 22325105, 52261135637 to D.S.), the Natural Science Foundation of Shandong Province (No. ZR2022QB008 to Z.W.), the National Postdoctoral Innovative Talents Support Program (No. BX2021171 to Z.W.), China Postdoctoral Science Foundation (No. 2021M700081 to Z.W.) and the Instrument Improvement Funds of Shandong University Public Technology Platform (ts20220102).

Author contributions

The original idea was conceived by D.S., experiments and data analyses were performed by Z.W., Y.-J.Z., B.-L.H., Y.-Z.L., C.-H.T., and D.S., ESI-MS data were collected by B.-L.H. and Y.-J.Z., structure characterization was performed by Z.W., Y.-J.Z., and D.S., the paper was drafted by D.S., Z.W., and Y.-J.Z. All authors have given approval to the paper.

Competing interests

The authors declare no competing interests.

Additional information

Supplementary information The online version contains supplementary material available at
<https://doi.org/10.1038/s41467-023-41050-x>.

Correspondence and requests for materials should be addressed to Di Sun.

Peer review information *Nature Communications* thanks the anonymous reviewers for their contribution to the peer review of this work. A peer review file is available.

Reprints and permissions information is available at
<http://www.nature.com/reprints>

Publisher's note Springer Nature remains neutral with regard to jurisdictional claims in published maps and institutional affiliations.

Open Access This article is licensed under a Creative Commons Attribution 4.0 International License, which permits use, sharing, adaptation, distribution and reproduction in any medium or format, as long as you give appropriate credit to the original author(s) and the source, provide a link to the Creative Commons licence, and indicate if changes were made. The images or other third party material in this article are included in the article's Creative Commons licence, unless indicated otherwise in a credit line to the material. If material is not included in the article's Creative Commons licence and your intended use is not permitted by statutory regulation or exceeds the permitted use, you will need to obtain permission directly from the copyright holder. To view a copy of this licence, visit <http://creativecommons.org/licenses/by/4.0/>.

© The Author(s) 2023